Optimization of multilayer Laue lenses for a scanning X-ray microscope

Hanfei Yan* and Yong S. Chu

National Synchrotron Light Source II, Brookhaven National Laboratory, Upton, NY 11973, USA.
E-mail: hyan@bnl.gov

Multilayer Laue lenses (MLLs) have demonstrated great capabilities for efficiently focusing hard X-rays down to the nanometer scale. Optimized use of MLLs in a scanning X-ray microscope requires careful consideration of a number of practical parameters other than resolution and efficiency in order to optimize the microscope's performance and scientific throughput. Here, relationships among the apodization effect owing to the presence of a beamstop, the monochromaticity requirement and the allowable working distance are discussed, as well as their impacts on the performance of the optics. Based on these discussions, optimal MLL schemes aiming at 10 nm resolution for a scanning X-ray microscope for the Hard X-ray Nanoprobe (HXN) beamline at National Synchrotron Light Source II are presented.

Keywords: X-ray; nanofocusing; multilayer Laue lens; apodization; monochromaticity.

1. Introduction

The unique properties of X-rays, for example, their penetration power, sensitivity to structural and chemical information, and insensitivity to electromagnetic fields, make them ideal nondestructive tools in many areas of science. The rapid growth of nanoscience in the last decade, which studies systems at the nanometer scale, engenders a strong demand for X-ray tools capable of high spatial resolution. One example is the study of solid-oxide fuel cells that have garnered much scientific and public attention as a clean energy source. It was shown that the microstructure of the fuel cell plays a critical role in determining its performance and durability (Faes *et al.*, 2009; Grew *et al.*, 2010; Suzuki *et al.*, 2009; Wilson *et al.*, 2006). It is crucial to understand the electrochemical reactions at the triple-phase boundary and electrolyzers, which requires knowledge of the changes in structure, elemental distribution and chemical state at the nanoscale during operation. Unfortunately, electron microscopy cannot easily access such information because of poor penetration power. On the other hand, scanning hard X-ray microscopy offers a nondestructive probing tool ideal for such studies. Currently, zone-plate (ZP)-, compound-refractive-lens (CRL)- or Kirkpatrick–Baez (KB) mirror-based scanning hard X-ray microscopy tools offer a two-dimensional spatial resolution in the range 40–300 nm for scientific applications (Bertoni *et al.*, 2011; Ding *et al.*, 2012; Hignette *et al.*, 2005; Ice *et al.*, 2011; Liu *et al.*, 2005a; Matsuyama *et al.*, 2006; Schroer *et al.*, 2010).

Multilayer Laue lenses (MLLs) are emerging nanofocusing optics with unique capabilities of efficiently focusing hard X-rays down to the nanometer scale (Kang *et al.*, 2006, 2008).

A MLL is fabricated by a thin-film deposition technique (Koyama *et al.*, 2008; Liese *et al.*, 2010; Liu *et al.*, 2005b), enabling accurate deposition control of a large number of alternating thin layers, whose thickness obeys the zone plate law in the direction normal to the surface. Thin-film deposition overcomes two major difficulties in fabricating a ZP by the conventional lithography method: achieving an outermost zone width well below 10 nm and a high aspect ratio. The former determines the size of the ZP focus and the latter determines its achievable efficiency. Thin zones, down to 0.7 nm, have been deposited by sputtering (Conley *et al.*, 2007), with an almost limitless aspect ratio. To date, MLLs have demonstrated below 20 nm line focus with over 30% efficiency at 20 keV (Kang *et al.*, 2008; Koyama *et al.*, 2011a), and, in theory, a capability of focusing below 1 nm (Yan *et al.*, 2007; Pfeiffer *et al.*, 2006; Schroer, 2006). A theoretical study on imperfections also revealed that interface roughness does not deter the achievement of a 1 nm focus with MLLs (Yan, 2009). More recently, MLLs were used to produce two-dimensional scanning fluorescence microscopy images with a 25 nm × 27 nm resolution, a 17% efficiency at ∼20 keV and a focusing stability over 72 hours (Yan *et al.*, 2011), demonstrating the great potential of MLL optics for scientific applications. Other attempts of fabricating circular multilayer lenses for two-dimensional focusing have been reported as well (Koyama *et al.*, 2011b, 2012). In this paper we restrict our discussions to linear types, since the use of circular types is more straightforward.

Although a MLL may be treated as a special ZP, it has its own characteristics that are very different from ZPs owing to the effect of dynamical diffraction (Yan *et al.*, 2007). MLLs with flat zones are usually operated in a tilted geometry

favoring Bragg diffraction, and typically utilize only a partial structure with less than 50% of the full aperture (Kang *et al.*, 2006, 2008). Consequently, the theoretical considerations and practical experience gained from using ZPs are insufficient in optimizing the performance of an X-ray microscope manipulating MLLs. Practical factors, such as the requirement for monochromaticity, the working distance and the aperture of the lens, must be carefully optimized for MLL optics, in order to assure the maximum scientific throughput. For instance, a long working distance is very desirable for accommodating a great variety of experiments. For given MLLs, this requires incorporating a large central beamstop that negatively impacts the focus peak shape and monochromaticity requirement. Favoring one aspect of the optical performance may entail the degradation of others. Here, we thoroughly discuss these technical considerations that will guide the construction of a MLL microscope with optimized performance.

Figure 1
(*a*) A scheme of an X-ray beam focused by a MLL with a central beamstop. Divergent orders (+) are not shown. The working distance is determined by the distance from the OSA to the focal plane. As shown in the graph, blocking the second order not the zeroth order (dotted OSA position) sets the maximum allowable working distance. (*b*) An X-ray beam focused by a partial MLL. A central beamstop is not necessary if the aperture of the incident beam is matched to the lens size. The maximum working distance is no longer limited by the second focusing order.

2. Working distance, apodization effect and monochromaticity

MLL optics have been discussed comprehensively in review articles (Macrander *et al.*, 2009; Yan *et al.*, 2010). Depending on their operational geometry and zone profile, MLLs are categorized into four different types: flat, tilted, wedged and curved. Here, we focus on the first three because they are successfully fabricated or feasible to fabricate. The flat and tilted MLLs are not fundamentally different; both consist of a large number (*i.e.* thousands) of alternating flat layers with their positions following the zone-plate law,

$$x_j^2 = j\lambda f + j^2\lambda^2/4, \qquad j = 1, 2, 3, \ldots, \qquad (1)$$

where λ is the wavelength and f is the focal length of the lens. The flat MLL is operated in the normal-incidence geometry like a ZP, while the tilted MLL has a tilting angle with respect to the incoming beam to satisfy the Bragg condition, in order to achieve higher efficiency at a particular range of zones. For a modest numerical aperture (NA), the second term on the right-hand side of (1) can be neglected, as will be the case in the following discussion.

Similar to a ZP, the MLL possesses multiple focusing orders. Fig. 1(*a*) shows focusing paths for different orders. Owing to the wave form that we choose and also being consistent with our previous work (Yan *et al.*, 2007, 2011), we use a negative sign for convergent (*i.e.* focusing) diffraction orders and a positive sign for divergent diffraction orders. For general microscopy applications, a central beam stop, along with an order-sorting 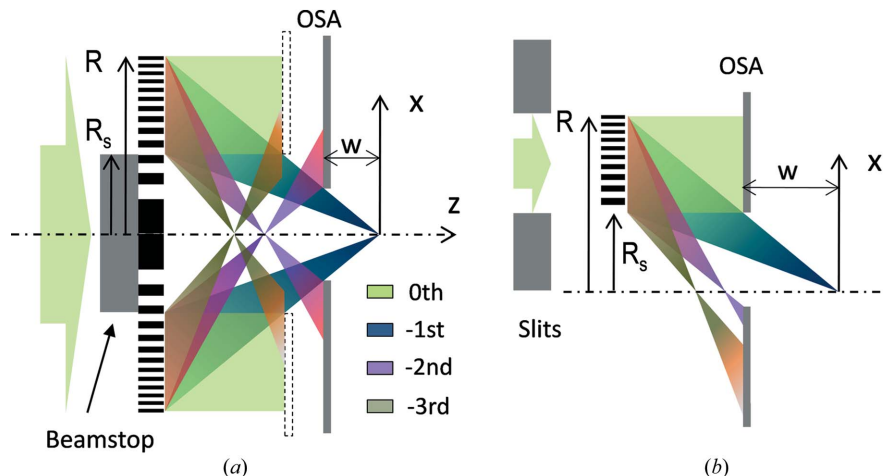aperture (OSA), must be used to block all unwanted beams from other orders at the focal plane of the desired order (Fig. 1*a*). Therefore, the working distance is no longer equal to the focal length. Instead, it is set by the distance from the OSA to the focal plane. The presence of the central beamstop creates two problems. It reduces the intensity of the central peak, and introduces strong side lobes, which is known as the apodization effect (Born & Wolf, 1999). In a real microscope, a long working distance is always preferable to broaden its range of applications, particularly those requiring significant space around the sample. As evident from the simple geometry shown in Fig. 1(*a*), many factors limit the working distance, *w*. If the first focusing order is desired, we can, for a full MLL, achieve the maximum working distance by blocking other orders without cutting off the first order,

$$\frac{w_h}{f} = \left|\frac{(h+1)\varepsilon}{(h\varepsilon - 1)}\right|, \quad h = 0, -2, -3, \ldots, \quad 0 \le \varepsilon = R_s/R < 1, \qquad (2)$$

where R_s and R are the radius of the central beamstop and the lens, respectively, and h is the order of diffraction. Because their wavefields are farther apart after the central beamstop, the positive orders do not need to be considered, as long as the zeroth order is blocked. We note that here the discussion is applicable to both the one-dimensional and two-dimensional cases, so the word 'radius' is used for generality. The working distance is limited by the smallest w_h at a given beamstop ratio, ε. For the zeroth order, w_0 is simply equal to εf. But, placing OSA at a distance εf away from the focal plane does not satisfy the requirement for blocking all high orders, as shown in Fig. 1(*a*). In Fig. 2 we plot the dependence of w_h on ε for different orders; it is evident that the second order places the most stringent requirement on the working distance. Though ideally even orders should have zero intensities and do not
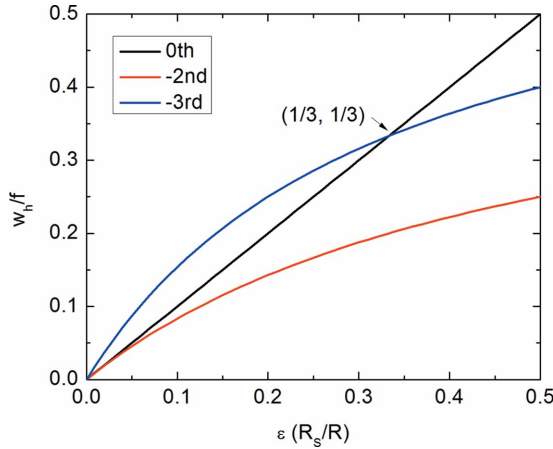
Figure 2
Maximum OSA-to-focal-plane distance allowed for blocking individual orders without cutting off the first order.

Figure 3
Top: crossed linear ZPs with a cross- and square-beamstop, and a conventional ZP with a circular beamstop. Bottom: their corresponding intensity distributions (linear scale) at the focal plane.

need to be considered, either a dynamical diffraction-effect (Yan *et al.*, 2007) or an imperfection (Yi *et al.*, 2011) in the diffractive lens can lead to a considerable even-order diffraction that needs to be blocked in practice. If ε is more than one-third, blocking the third order also requires w to be smaller than εf. Nevertheless, w increases with ε, although the relationship may not be linear.

A concern for a large ε is the apodization effect that results in strong side lobes owing to the interference of waves emerging from the two halves separated by the central beamstop. For simplicity, we neglect any dynamical-diffraction effect and assume that the lens has a constant pupil function. For a point focus formed by two crossed one-dimensional lenses, there are two different scenarios depending on the shape of the central beamstop. One is a cross beamstop, formed by two cross lines blocking the central part of an individual one-dimensional lens. The other is a square beam-stop, blocking only the central part of the crossed lenses. The intensity distribution at the focal plane in the former case is

$$I(\varepsilon, X, Y) = \frac{I_0}{(1-\varepsilon)^4}\left[\frac{\sin(X)}{X} - \frac{\sin(\varepsilon X)}{X}\right]^2\left[\frac{\sin(Y)}{Y} - \frac{\sin(\varepsilon Y)}{Y}\right]^2,$$

(3)

where $X = 2\pi Rx/\lambda f$, $Y = 2\pi Ry/\lambda f$, and that in the latter case is

$$I(\varepsilon, X, Y) = \frac{I_0}{(1-\varepsilon^2)^2}\left[\frac{\sin(X)\sin(Y)}{XY} - \frac{\sin(\varepsilon X)\sin(\varepsilon Y)}{XY}\right]^2.$$

(4)

Here I_0 is the intensity at the focal spot $[I_0 = I(\varepsilon, 0, 0)]$, and X and Y are dimensionless Cartesian coordinates. We can compare these expressions with that for a circular zone plate,

$$I(\varepsilon, \rho) = \frac{I_0}{(1-\varepsilon^2)^2}\left[\frac{2J_1(\rho)}{\rho} - \frac{2\varepsilon J_1(\varepsilon\rho)}{\rho}\right]^2,$$

(5)

where $\rho = 2\pi Rr/\lambda f$ and J_1 is the first-order Bessel function. Here ρ is the dimensionless radius. Fig. 3 shows geometries corresponding to equations (3)–(5), and the expected intensity distribution at the focal plane in their respective cases. The
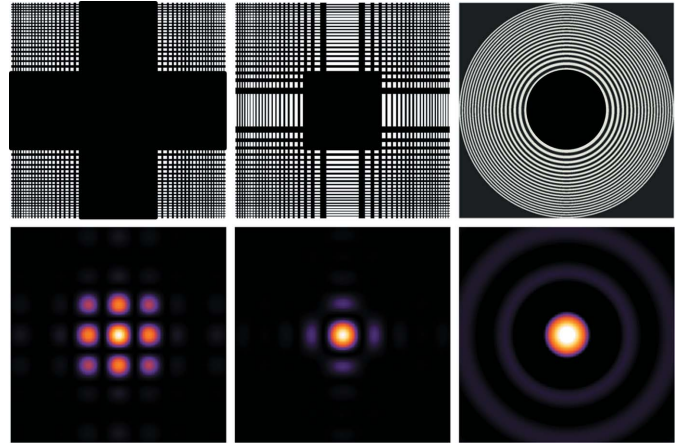
ratio of the unblocked area to the total area of the full structure is equal to $(1-\varepsilon)^2$ in the first case, and $(1-\varepsilon^2)$ in the latter two. Introducing a central beamstop engenders an increase of the side lobe but a decrease of the distance of the first zero to the origin, a feature that sometimes is utilized to achieve super-resolution for visible light (Sales & Morris, 1997*a,b*). This is depicted in Fig. 4(*a*). However, for an X-ray scanning microscope, the reduction of the width of the central peak may not entail better resolution since the intensity of the excited fluorescence is proportional to the total number of photons in the focus. If the side lobes contain more photons, the footprint of the signal will be increased. It may be more meaningful to discuss the fraction of the total energy within the central peak, which is plotted in Fig. 4(*b*). As is evident, the cross beamstop results in the steepest decrease as ε increases. An ε value of 0.25 is often used in X-ray scanning microscopes equipped with a circular ZP. From Fig. 4(*b*), this corresponds to 73% of the focused photons in the central peak. For two crossed MLLs with a square beamstop, there is a small difference compared with that of the circular ZP. On the other hand, if a cross beamstop is used, the fraction of energy in the central peak declines to 33%. Maser and colleagues (Maser *et al.*, 2004) first discussed this scenario and showed a similar result. To assure a similar fraction of energy in the central peak, an ε value smaller than 0.05 is needed for a cross beamstop, resulting in an extremely small working distance. The square beamstop, though superior to the cross beamstop, is more difficult to implement in practice, owing to the fact that two MLLs are involved.

A simple solution for these problems is to use only one side of the MLL, or, in other words, a partial MLL (Fig. 1*b*). There are three immediate benefits. The first is the working distance, which is no longer limited by the second order but is directly proportional to the ratio of the size of the central beamstop to that of the lens, $w = \varepsilon f$. The second is the disappearance of the apodization effect, since equation (3) is reduced to the square of a single sinc function, independent of ε. Moreover, because the thinner zones are always grown first for a MLL, a central
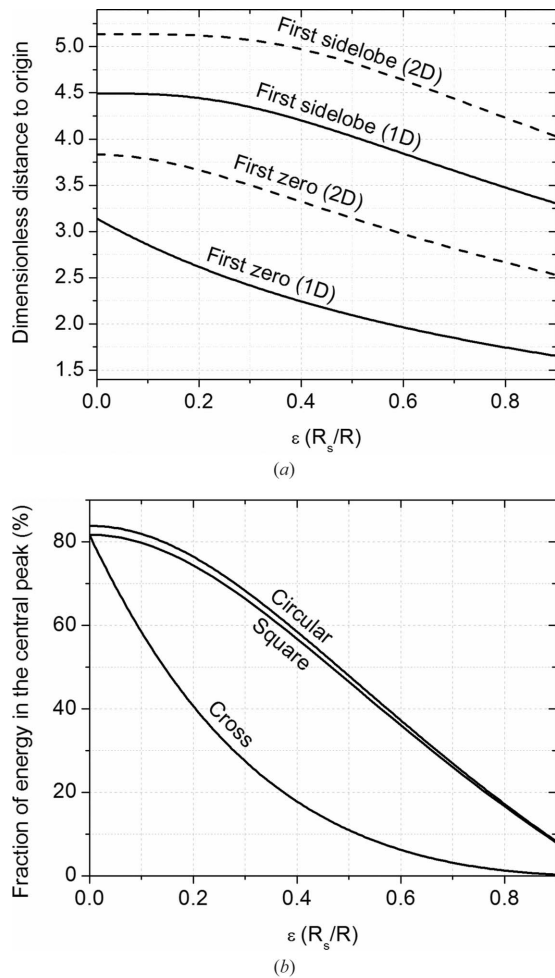
Figure 4
(a) Changes of the first zero and the first side-lobe positions in one-dimensional and two-dimensional (circular ZP) cases, as a function of the beamstop ratio, ε. (b) Dependence of the total energy within the central peak on the beamstop ratio, ε. The three cases are shown in Fig. 3.

beamstop is not required if central zones are not grown and the incident beam is restricted only to the lens aperture using slits. An obvious disadvantage of using a partial MLL is that more zones must be deposited to achieve the same NA. This observation poses a question. Does this have a negative impact on the requirement for monochromaticity? In other words, is a higher monochromaticity needed for a partial MLL as compared with a full structure with the same NA?

To answer this question, we revisited the thin-lens formula. It is well known that the monochromaticity requirement for ZPs is inversely proportional to the number of zones (Attwood, 1999). This can be understood by the chromatic nature of a diffractive optic: its focal length changes proportionally with the energy of the incident X-ray beam. To avoid chromatic blurring owing to a finite energy bandwidth, we make sure that the associated difference in the focal length should not be larger than the depth of focus (DOF). As a result we arrive at

$$\frac{\pm\Delta E/2}{E} = \frac{\text{DOF}}{f}, \qquad \text{DOF} = \pm\frac{\lambda}{2\text{NA}^2}. \qquad (6)$$

By combining with (1), we can simplify (6) to the well known relationship

$$\Delta E/E = 1/N_Z, \qquad (7)$$

where N_Z is the number of zones. For a one-dimensional ZP, N_Z is equal to the number of the zones on only one side.

Now let us look back to MLLs. The total number of zones deposited for a partial MLL with a beamstop ratio $\varepsilon = R_s/R$ and a lens size of $S = R - R_s$ satisfies the equation

$$N_Z = \frac{S^2}{\lambda f}\frac{1+\varepsilon}{1-\varepsilon}. \qquad (8)$$

If S, λ and f are constants, a change of ε from 0 to 0.5 results in tripling N_Z. Equation (6) states that the monochromaticity requirement would not change, since DOF is the same. But, according to (7), this is not the case. Solving this discrepancy boils down to the question of whether there is more fundamental physics associated with (7).

We may consider this problem from a different perspective. Monochromaticity is related to longitudinal coherence. To achieve a diffraction-limited focus, all X-rays travelling along different paths must be both transversely coherent and longitudinally coherent. The latter requires that the maximum difference in the optical path does not exceed the longitudinal coherence length determined by the energy bandwidth of the incoming beam. Conventionally, this length is defined as $\lambda^2/2\Delta\lambda$, at which two waves with a wavelength difference of $\Delta\lambda$ will experience a π phase difference, *i.e.* they are completely out of phase (Attwood, 1999). For an incident plane wave, a ZP is designed in such a way that the increment in the optical path to the focus of a pencil ray emerging from the jth zone is $j(\lambda/2)$ compared with that of the central ray. This is evident by considering a pencil ray emerging at position x_j. The optical path to the focus is larger than that of the central ray through the origin by an amount $(x_j^2 + f^2)^{1/2} - f \simeq x_j^2/2f$. The resulting phase change is $\pi x_j^2/\lambda f$. By combining with (1), we easily conclude that every increment in zone number corresponds to a half-wavelength increase in the optical path to the focus. Accordingly, the maximum difference in optical path in a ZP (or an MLL) is equal to the number of zones multiplied by the half-wavelength. If we set it equal to the longitudinal coherence length, we arrive at (7). Therefore, to avoid chromatic aberration, the energy bandwidth should not be larger than the inverse of the number of zones that determine the maximum optical-path difference to the focus.

The contradictory to the thin-lens formula [equation (6)], which, at first glance, also should be correct, can be understood by looking at Fig. 5. It illustrates intensity distributions near the focus corresponding to two incident plane waves with slightly different energy. Because of the difference in wavelength, the focus spots corresponding to the two energies are different along the optical axis, labelled B. Owing to the partial structure, as shown *via* this simulation, the direction of the DOF is along the inclined axis A; the DOF is not changed as long as the NA remains the same, if we neglect the small change in wavelength. However, the focus shift owing to an
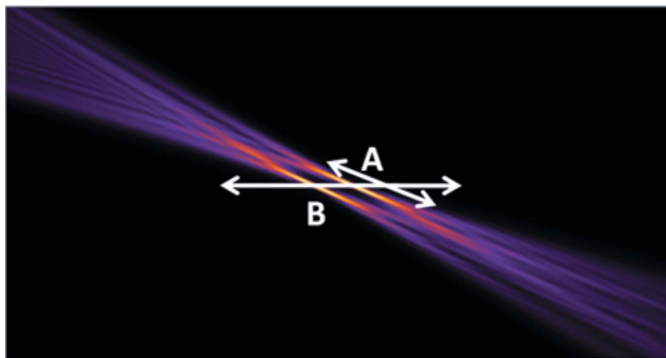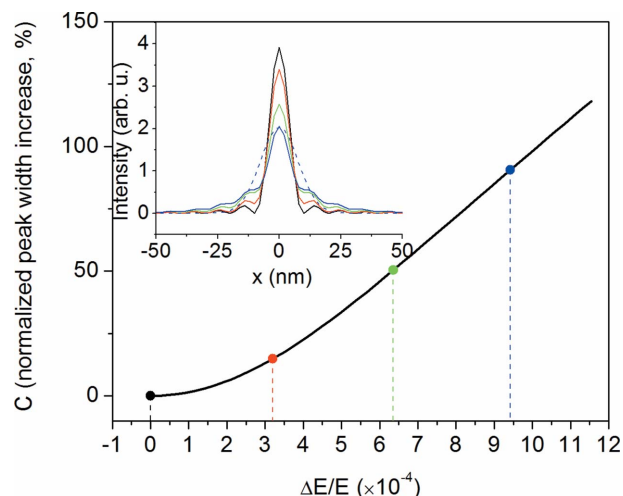
Figure 5
The intensity distributions near the focus of a partial MLL for two incident plane waves with slightly different energy. The focus shifts along the optical axis *B*, while the depth of focus is along axis *A*.

Figure 6
The dependence of the normalized focus-broadening for a full MLL on the energy bandwidth of the incident beam. The inset shows focus profiles at specific energy bandwidths denoted by colored dots. The equivalent Gaussian fit (dashed blue curve) to the focus profile (solid) is overlaid for a comparison purpose.

energy change is along axis *B*, not axis *A*. The drop in intensity is much steeper along axis *B* than that along axis *A*. Consequently, we cannot equate the change in focal length to the DOF in assessing the energy tolerance for a partial MLL. A geometrical factor has to be taken into account. Certainly, the more inclined axis *A* is (the higher ε), the more sensitive is the focus size to an energy spread, in agreement with the longitudinal-coherence argument. In summary, equation (6) only works for an 'on-axis' optic where the propagation direction of the focus beam is the same as that of the incident beam.

Based on this observation, we draw some interesting conclusions that may not be intuitive. One, a half MLL with the half NA will have the same monochromaticity requirement as that for a full MLL because the optical-path difference is the same. Two, for the same NA, the bigger ε is, the higher the monochromaticity must be since more zones are needed. To clarify these effects, we conduct a numerical simulation. The MLL considered here has a focal length of 10 mm at 10 keV and a NA of 6.2 mrad. A diffraction-limited spot size of 10 nm (Rayleigh criterion) is expected. We start by considering the simplest case, a full MLL with $\varepsilon = 0$. The number of zones (one side) is 3100, leading to a monochromaticity requirement of 3.2×10^{-4}. For an incident beam with a normalized Gaussian energy distribution, it is convenient to calculate the decrease of the peak intensity, $I(0, \Delta E)/I(0, 0)$, as a function of the $\Delta E/E$ ratio, where ΔE is the full width at half-maximum (FWHM) of the energy spread. If the total number of incoming photons remains the same and the focus peak is approximated to a Gaussian function, the normalized peak width broadening can be defined as

$$C(\Delta E) = \frac{I(0, 0)}{I(0, \Delta E)} - 1. \qquad (9)$$

This quantity serves as a good estimate of the focus-broadening effect due to an energy bandwidth, provided that the shape of the focus peak does not deviate markedly from a Gaussian function. In Fig. 6 we plot the normalized peak width broadening as a function of incoming X-ray monochromaticity, assuming a Gaussian distribution. As is evident, for a small energy spread, the peak width remains nearly

unchanged. Then, it starts to increase almost linearly after a certain value. The colored dots correspond to bandwidths equal to 0, 3.2×10^{-4}, 6.4×10^{-4} and 9.4×10^{-4}. At the position of the red dot (3.2×10^{-4}), the focus broadening is 15%. It becomes 52% and 91% at the positions of the green and blue dots. In the inset, we also show the simulated focus profiles corresponding to monochromaticities marked by different colors. The dashed curve in blue is a Gaussian profile equivalent to the actual focus profile (solid in blue) with the same total area underneath, shown for comparison. It is noteworthy that, as the energy bandwidth increases, the central peak does not broaden appreciably, in this case. On the other hand, the side lobes are enhanced and broadened quickly, so that less energy is contained within the central peak. Fitting only the central peak by a Gaussian, the peak profile changes its FWHM (note FWHM will yield a slightly smaller diffraction-limited focus size compared with the Rayleigh criterion) from 8.5 nm to 9 nm, 10 nm and 11 nm, respectively. The energy fraction of the central peak decreases from 91% to 84%, 72% and 62% at three different energy bandwidths highlighted by the colored dots. If side lobes become dominant, the FWHM of the central peak may not be a good measure to quantify the size of the focus. The quantity *C* defined here represents the change of the integral width of the focus, which is more appropriate for microscopy applications.

For a partial MLL, it is still true that, at the focal plane, the peak position is at the origin, so we can still use the normalized focus-broadening to depict the increase in the peak width. In Fig. 7, we plot the changes of this quantity for partial MLLs with $\varepsilon = 0$ and $\varepsilon = 0.2$ as the energy bandwidth increases, along with that for the full MLL. The two partial MLLs have the same NA (a diffraction-limited focus size of 20 nm, Rayleigh criterion), *viz.* the half of the full MLL (a diffraction-limited focus size of 10 nm). Simulation results confirm our predic-
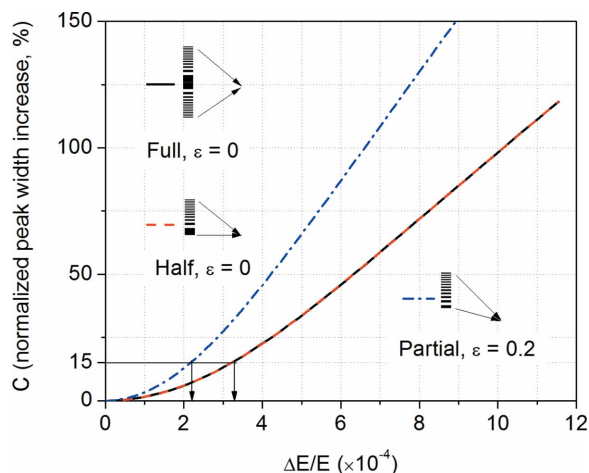
Figure 7
The normalized focus-broadening in three different cases: a full MLL ($\varepsilon = 0$); a half MLL of the first one ($\varepsilon = 0$, half NA of the first one); and a partial MLL having the same NA as the second one ($\varepsilon = 0.2$). The arrows show the corresponding energy bandwidth when the peak is broadened by 15%.

tions, based on the longitudinal coherence argument. The partial MLL with high ε value requires a high monochromaticity, even though their NA is the same. Setting $C = 15\%$ as the threshold for the partial MLL with $\varepsilon = 0.2$, the required monochromaticity is 2.13×10^{-4}, equal to the inverse of the number of zones of 4650. For the partial MLL with $\varepsilon = 0$, its normalized peak width broadening is identical to that of the full MLL with a doubled NA.

3. Dynamical diffraction effects of MLLs

The discussion above is general but does not take into account the unique dynamical diffraction-properties of MLLs. Here, we consider more realistic conditions and present our optics design approach for the microscope. Utilizing a partial MLL offers important optical advantages, although more zones with smaller zone width must be deposited to achieve the same NA. The necessity to produce thinner zone width for a partial MLL does not pose a significant fabrication challenge, since fabricating thin zones down to 0.7 nm have been successful (Conley et al., 2007). However, the total number of zones must be carefully considered, in order to work effectively with the given monochromaticity of the incident beam and the level of dynamical diffraction.

MLLs diffract X-rays dynamically, in most cases. The smaller the zone width, the stronger the dynamical-diffraction effect. In the one-dimensional case, the focus size (Rayleigh criterion) is equal to the width of the outermost zone of a full MLL. For a partial MLL, the outermost zone width is reduced by a factor, $(1 - \varepsilon)/2$, to achieve the same spot size as for the full MLL. For example, if we use $\varepsilon = 0.5$, the width of the outermost zone of a partial MLL must be 2.5 nm for a diffraction-limited 10 nm focus because its NA is only a quarter of the corresponding full MLL. With a decrease in zone width, the effect of dynamical diffraction becomes

increasingly dominant, resulting in a narrow diffraction efficiency profile across the lens at the exit MLL surface or the pupil plane. This will limit the effective NA. The pupil function of the lens is no longer a constant over the aperture. At the pupil plane of an MLL, the diffraction intensity will be low except in the vicinity of the zones where the Bragg condition is satisfied. Consequently, even if the physical size of a partial MLL is sufficiently large, the dynamical-diffraction effects will prevent it from achieving a diffraction-limited spot. The black solid line in Fig. 8 indicates the first-order diffraction intensity of a partial MLL with flat zone at the pupil plane. The partial MLL has an ε value of 0.5, zones ranging from 2.5 nm to 5 nm wide, and a section depth (thickness along the optical axis) of 10.6 µm, corresponding to a π phase change in two adjacent zones at 20 keV. The MLL is tilted to the incident beam by an angle of $0.25°$. As is apparent from the simulation, the pupil function of this MLL depicts a strong peak decorated with many side lobes emerging at the position where the Bragg condition is satisfied. Although the peak intensity is very high, its width is confined into a small region. Moreover, a more than π phase-change occurs across the diffraction peak, making waves emerging from different parts of the lens out of phase at the focus. The lens suffers from not only a reduced effective NA, but also a strong phase aberration. The focus of this lens at the focal plane (inset) is broadened and severely distorted compared with the diffraction-limited focus.

Two different approaches can be taken to overcome this difficulty. One is to reduce the section depth of the MLL so that the dynamical-diffraction effect is weaker. However, this choice would decrease efficiency. A trade-off must be made between the working distance (large ε preferred), the effective
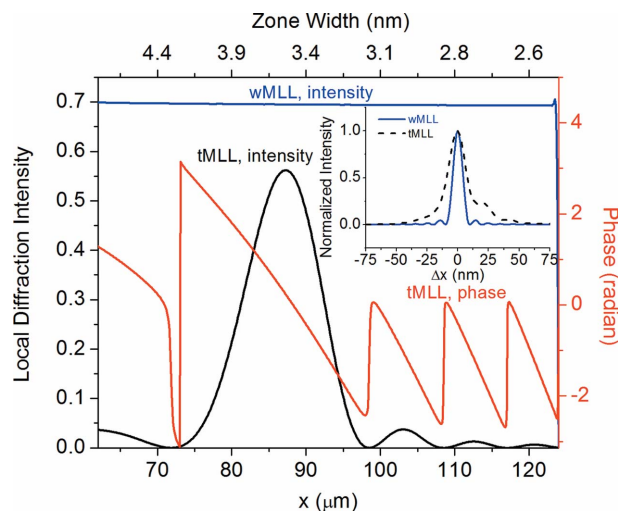

Figure 8
The local diffraction intensity across a tMLL and wMLL with $\varepsilon = 0.5$ at the pupil plane. The MLL size is 62 µm, and the zone width varies from 2.5 to 5 nm. The tilting angle is $0.25°$ for the tMLL and $0°$ for the wMLL. The section depth is 10.6 µm for the tMLL (to achieve π phase change in two adjacent zones) and 16.5 µm (to achieve an optimal efficiency accounting for dynamical-diffraction effect) for the wMLL. The red curve shows the corresponding phase of the pupil function of the tMLL. The simulation was performed at 20 keV. For a focal length of 10 mm, the diffraction-limited focus size is 10 nm. The inset shows the focus profile for each case.

Table 1
Lens parameters for tMLLs and wMLLs designed to work at 10 and 20 keV for a 10 nm focus.

The parameters are focal length (f), beamstop ratio (ε), working distance (w), aperture size (S), outermost zone width (dr_o), inner most zone width (dr_i), number of zones (N_Z), monochromaticity ($\Delta E/E$), section depth (t_{dep}) and efficiency.

	f (mm)	ε (R_s/R)	w (mm)	S (µm)	dr_o–dr_i (nm)	N_Z	$\Delta E/E$ ($\times 10^{-4}$)	Si (111) ($\times 10^{-4}$)	t_{dep} (µm)	Efficiency (1D, %)
tMLL (10 keV)	5	0.2	1	62	4–20	9300	1.1	$\sim$1.3	4	15
wMLL (10 keV)	2.57	0.414	1.1	31.9	2.9–7.1	7690	1.3		9.5	69
tMLL (20 keV)	10	0.2	2	62	4–20	9300	1.1	$\sim$1.3	8	20
wMLL (20 keV)	5.14	0.414	2.1	31.9	2.9–7.1	7690	1.3		16.5	69

NA and the efficiency (small ε preferred). Another approach is to grow wedged MLLs (wMLLs), for which the dynamical effect is favorable for both. Efficiency is significantly enhanced and the effective NA is not limited by small zones, because the Bragg condition is sufficiently satisfied across all the zones. We also simulated the local diffraction intensity of a wMLL with identical parameters as the tMLL (hereafter referred to as tiled MLLs with flat zones) in Fig. 8, except the section depth is increased to 16.5 µm for optimal efficiency accounting for the dynamical-diffraction effect. A high and almost constant diffraction-intensity profile is observed across the lens. The focus profile of this wMLL, depicted in the inset, shows a diffraction-limited peak. This solution certainly is superior to reducing the lens section depth. Feasibility of depositing a wMLL with an appropriate zone profile has been demonstrated (Conley *et al.*, 2008), and on-going efforts are underway toward this grand challenge.

4. MLLs for an X-ray microscope with 10 nm spatial resolution

In the previous sections, we discussed how individual optical parameters affect the performance of MLL optics. Here, we discuss how these parameters are optimized to deliver a balanced performance for a real X-ray microscope. For a real X-ray microscope, we need to ensure an adequate working distance for diverse experiments and sufficiently high focused flux for practical measurement throughput, in addition to a high spatial resolution. One important factor in optimizing the microscope performance is the monochromaticity ($\Delta E/E$) limit. Most synchrotron beamlines use a Si (111) double-crystal monochromator (DCM), with intrinsic monochromaticity of $\sim$1.3 $\times$ 10^{-4} in the energy range 10–20 keV. Consequently, it is important to ensure that the MLL parameters are designed to work within the beamline monochromaticity. For a 10 nm spatial resolution, the MLLs can be designed to work with the monochromaticity of a Si (111) DCM, while providing an adequate amount of working distance and sufficiently high focused flux. As an example of optimization, we present the MLL optical parameters designed for the Hard X-ray Nanoprobe (HXN) of National Synchrotron Light Source II (NSLS-II). The NSLS-II's HXN is currently being constructed to offer a 10 nm spatial resolution by implementing MLL optics in its scanning X-ray microscope (HXN Preliminary Design Report, http://www.bnl.gov/nsls2/project/).

Table 1 summarizes the optical parameters for tMLLs and wMLLs at 10 and 20 keV aiming at a 10 nm focus. Note that these parameters are developed for the use of partial MLLs, to avoid the apodization effect. Let us focus on the tMLLs first. For a full MLL, the requirement for a diffraction-limited focus of 10 nm sets the outermost zone width, dr_o, to be 10 nm. For a partial MLL, the beamstop ratio, ε, gives a more stringent requirement of dr_o, because thinner zones have to be deposited to achieve the same NA. For example, use of a 40% structure (*i.e.* $\varepsilon = 0.2$) results in $dr_o = 4$ nm. While a small beamstop ratio leads to a fewer number of zones [equation (8)], it reduces the working distance (see Fig. 2). On the other hand, a large beamstop ratio results in a small value of dr_o and dr_i, which increases the dynamical-diffraction effect. We choose a partial MLL with a focal length of 5 mm and a lens size of 62 µm at 10 keV, and a partial MLL with a focal length of 10 mm and a lens size of 62 µm at 20 keV to achieve a diffraction-limited focal size of 10 nm. The ε value is limited to 0.2, so that the outermost zone width is no smaller than 4 nm and the dynamical-diffraction effect is still manageable. The working distance is 1 mm and 2 mm at respective energies. Both lenses consist of 9300 zones and hence a monochromaticity requirement of $\sim$1.1 $\times$ 10^{-4}. This value is slightly smaller than that given by the standard Si (111) monochromator, *i.e.* $\sim$1.3 $\times$ 10^{-4} in the energy range 10–20 keV. We choose a section depth of 4 µm at 10 keV and 8 µm at 20 keV for MLLs consisting of Si and WSi$_2$ layers. A small section depth, though not optimized for efficiency, is selected to avoid a strong dynamical-diffraction effect and to avoid the loss of the effective NA. The calculated efficiency for individual MLLs is 15% and 20%, respectively. The overall efficiency for two MLLs in a cross geometry is 2% and 4% at 10 keV and 20 keV, respectively. To clarify the chromatic blurring effect due to N_Z = 9300, we plot in Fig. 9 the simulated focus profile by assuming an incident beam with a Gaussian energy distribution. The FWHM of the energy bandwidth is set to 1.3 $\times$ 10^{-4}. From this simulation, for given MLLs at their respective energy, the FWHM of the peak is increased to 11 nm. We choose to accept this small amount of chromatic blurring, in order to achieve a larger working distance and higher efficiency.

Let us consider the case for wMLLs. The wMLL gives a significantly higher efficiency, in comparison with tMLLs. In addition, the dynamical-diffraction effect is no longer a limiting factor on the achievable NA, even for thin zones. Therefore, ε is not limited to a small value and we can increase
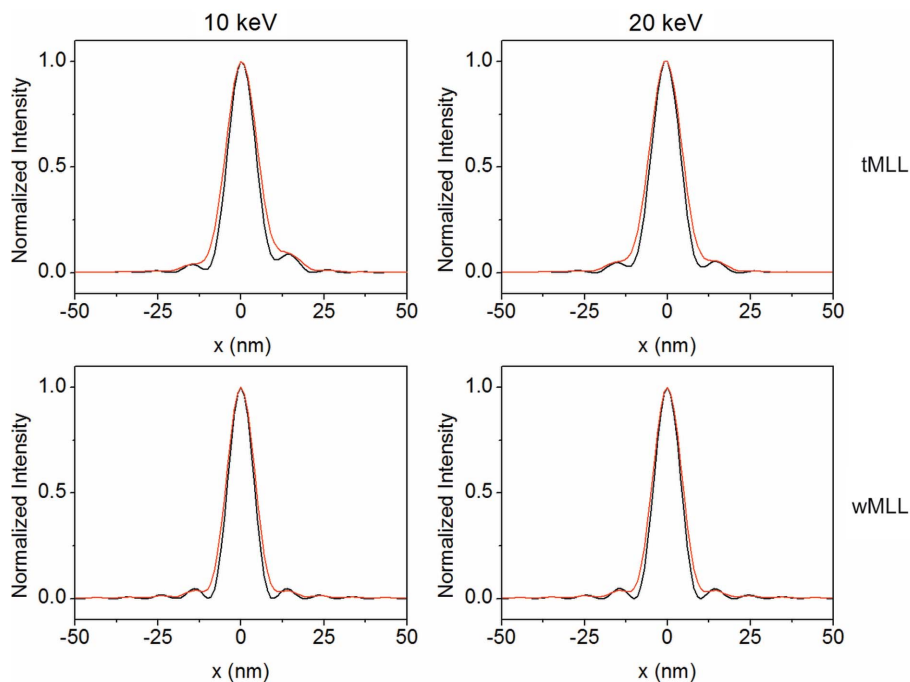
Figure 9
Focus profiles of a tMLL (top panel) and a wMLL (bottom panel) for an incident monochromatic beam (black) and chromatic beam (red) at 10 keV (left column) and 20 keV (right column). Lens parameters are given in Table 1.

it to optimize all parameters. We can rewrite equation (8) as

$$\frac{N_Z\lambda}{(2NA)^2 w} = \frac{1+\varepsilon}{\varepsilon(1-\varepsilon)}. \quad (10)$$

At given energy, the above combination of NA, the working distance and the number of zones depends only on ε. Fig. 10 shows how the value of this combination is dependent on ε (see solid black line). A minimum value of 5.83 is reached when we have $\varepsilon = \sqrt{2} - 1$. This sets the maximum working

Figure 10
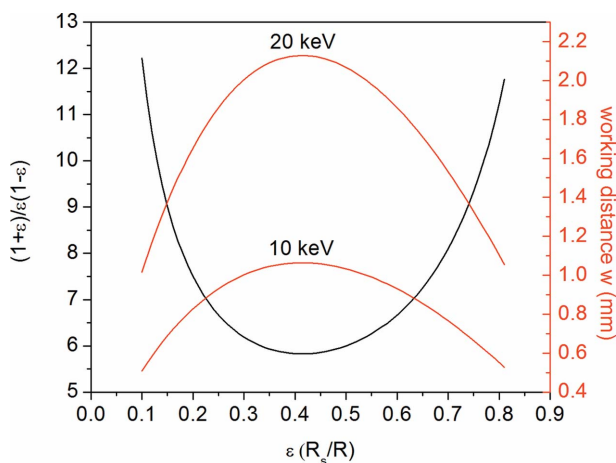Variations of the ε-dependent term in equation (10) (black) and the corresponding working distance at 10 and 20 keV (red) when the lens monochromaticity requirement is matched to the energy bandwidth of a Si (111) monochromator. The diffraction-limit focus size of the lens is 10 nm.

distance achievable for a given focus size when the lens' requirement for monochromaticity is matched to the energy bandwidth determined by the Si (111) monochromator. For a 10 nm focus, this maximum working distance is 1.1 mm at 10 keV, and 2.1 mm at 20 keV (see red curves in Fig. 10). The corresponding focal length and lens size are 2.6 mm and 31.9 µm at 10 keV, 5.1 mm and 31.9 µm at 20 keV. Table 1 summarizes these optimized parameters at 10 and 20 keV. Because the curve shown in Fig. 10 varies very slowly around the bottom, we can tailor the value of ε to have the correct lens size matched to the coherence length of a given beamline, by paying only a small penalty in the working distance. For example, if we choose $\varepsilon = 0.3$, the lens size is increased to 37.2 µm for a 10 nm focus at 10 keV, while the working distance is reduced to 1 mm.

To confirm that a 10 nm focus can be achieved by the wMLLs with the parameters shown in Table 1, we conducted a simulation assuming an incident beam with an energy bandwidth of 1.3×10^{-4}. The results are depicted in Fig. 8. There is still a marginal broadening ($\sim$1 nm) owing to the energy bandwidth compared with the case of a monochromatic beam. High efficiency of $\sim$69% can be achieved both at 10 and 20 keV, resulting in an overall two-dimensional efficiency over 45%. For all above simulations we assume the incident beam is fully coherent in the transverse direction.

5. Conclusion

In summary, we studied the apodization effect, the monochromaticity requirement and the working distance of MLL optics. We detailed the relationship and dependence among them, as well as their impacts on the lens performance. Our studies showed that partial MLL structures were preferable for achieving a long working distance and minimizing the apodization effect. However, using partial MLLs has an adverse impact on the requirement of monochromaticity, and careful optimization is required for designing MLL optics for a real X-ray microscope. As a concrete example, we presented the detailed explanation on the lens parameters designed for a scanning X-ray microscope at the Hard X-ray Nanoprobe of the NSLS-II. Our study demonstrates that a 10 nm focus is readily achievable by partial MLLs with manageable dynamical-diffraction effect and chromatic aberration with a standard monochromator.

References

Attwood, D. T. (1999). *Soft X-rays and Extreme Ultraviolet Radiation: Principles and Applications.* Cambridge University Press.

Bertoni, M. I., Fenning, D. P., Rinio, M., Rose, V., Holt, M., Maser, J. & Buonassisi, T. (2011). *Energy Environ. Sci.* **4**, 4252–4257.

Born, M. & Wolf, E. (1999). *Principles of Optics.* Cambridge University Press.

Conley, R., Liu, C., Kewish, C. M., Macrander, A. T. & Morawe, C. (2007). *Proc. SPIE*, **6705**, 670505.

Conley, R., Liu, C., Qian, J., Kewish, C. M., Macrander, A. T., Yan, H., Kang, H. C., Maser, J. & Stephenson, G. B. (2008). *Rev. Sci. Instrum.* **79**, 053104.

Ding, Y., Cai, Z. H., Hu, Q. Y., Sheng, H. W., Chang, J., Hemley, R. J. & Mao, W. L. (2012). *Appl. Phys. Lett.* **100**, 4.

Faes, A., Hessler-Wyser, A., Presvytes, D., Vayenas, C. G. & Van Herle, J. (2009). *Fuel Cells*, **9**, 841–851.

Grew, K. N., Chu, Y. S., Yi, J., Peracchio, A. A., Izzo, J. R., Hwu, Y., De Carlo, F. & Chiu, W. K. S. (2010). *J. Electrochem. Soc.* **157**, B783–B792.

Hignette, O., Cloetens, P., Rostaing, G., Bernard, P. & Morawe, C. (2005). *Rev. Sci. Instrum.* **76**, 063709.

Ice, G. E., Budai, J. D. & Pang, J. W. (2011). *Science*, **334**, 1234–1239.

Kang, H. C., Maser, J., Stephenson, G. B., Liu, C., Conley, R., Macrander, A. T. & Vogt, S. (2006). *Phys. Rev. Lett.* **96**, 127401.

Kang, H. C., Yan, H. F., Winarski, R. P., Holt, M. V., Maser, J., Liu, C. A., Conley, R., Vogt, S., Macrander, A. T. & Stephenson, G. B. (2008). *Appl. Phys. Lett.* **92**, 221114.

Koyama, T., Ichimaru, S., Tsuji, T., Takano, H., Kagoshima, Y., Ohchi, T. & Takenaka, H. (2008). *Appl. Phys. Express*, **1**, 117003.

Koyama, T., Takano, H., Konishi, S., Tsuji, T., Takenaka, H., Ichimaru, S., Ohchi, T. & Kagoshima, Y. (2012). *Rev. Sci. Instrum.* **83**, 013705.

Koyama, T., Takenaka, H., Ichimaru, S., Ohchi, T., Tsuji, T., Takano, H. & Kagoshima, Y. (2011a). *AIP Conf. Proc.* **1365**, 24–27.

Koyama, T., Tsuji, T., Takano, H., Kagoshima, Y., Ichimaru, S., Ohchi, T. & Takenaka, H. (2011). *AIP Conf. Proc.* **1365**, 100–103.

Liese, T., Radisch, V. & Krebs, H. U. (2010). *Rev. Sci. Instrum.* **81**, 073710.

Liu, C., Conley, R., Macrander, A. T., Maser, J., Kang, H. C., Zurbuchen, M. A. & Stephenson, G. B. (2005b). *J. Appl. Phys.* **98**, 113519.

Liu, W., Ice, G. E., Tischler, J. Z., Khounsary, A., Liu, C., Assoufid, L. & Macrander, A. T. (2005a). *Rev. Sci. Instrum.* **76**, 113701.

Macrander, A. T., Yan, H., Kang, H. C., Maser, J., Liu, C., Conley, R. & Stephenson, G. B. (2009). In *Handbook of Optics*, Vol. V. New York: McGraw-Hill Professional.

Maser, J., Stephenson, G. B., Vogt, S., Wenbing, Y., Macrander, A., Kang, H. C., Chian, L. & Conley, R. (2004). *Proc. SPIE*, **5539**, 185–194.

Matsuyama, S., Mimura, H., Yumoto, H., Sano, Y., Yamamura, K., Yabashi, M., Nishino, Y., Tamasaku, K., Ishikawa, T. & Yamauchi, K. (2006). *Rev. Sci. Instrum.* **77**, 103102.

Pfeiffer, F., David, C., van der Veen, J. F. & Bergemann, C. (2006). *Phys. Rev. B*, **73**, 245331.

Sales, T. R. M. & Morris, G. M. (1997a). *J. Opt. Soc. Am. A*, **14**, 1637–1646.

Sales, T. R. M. & Morris, G. M. (1997b). *Opt. Lett.* **22**, 582–584.

Schroer, C. G. (2006). *Phys. Rev. B*, **74**, 033405.

Schroer, C. G., Boye, P., Feldkamp, J. M., Patommel, J., Samberg, D., Schropp, A., Schwab, A., Stephan, S., Falkenberg, G., Wellenreuther, G. & Reimers, N. (2010). *Nucl. Instrum. Methods Phys. Res. A*, **616**, 93–97.

Suzuki, T., Hasan, Z., Funahashi, Y., Yamaguchi, T., Fujishiro, Y. & Awano, M. (2009). *Science*, **325**, 852–855.

Wilson, J. R., Kobsiriphat, W., Mendoza, R., Chen, H. Y., Hiller, J. M., Miller, D. J., Thornton, K., Voorhees, P. W., Adler, S. B. & Barnett, S. A. (2006). *Nat. Mater.* **5**, 541–544.

Yan, H. F. (2009). *Phys. Rev. B*, **79**, 165410.

Yan, H., Kang, H. C., Conley, R., Liu, C., Macrander, A. T., Stephenson, G. B. & Maser, J. (2010). *X-ray Opt. Instrum.* **2010**, 401854.

Yan, H. F., Maser, J., Macrander, A., Shen, Q., Vogt, S., Stephenson, G. B. & Kang, H. C. (2007). *Phys. Rev. B*, **76**, 115438.

Yan, H., Rose, V., Shu, D., Lima, E., Kang, H. C., Conley, R., Liu, C., Jahedi, N., Macrander, A. T., Stephenson, G. B., Holt, M., Chu, Y. S., Lu, M. & Maser, J. (2011). *Opt. Express*, **19**, 15069–15076.

Yi, J., Chu, Y. S., Chen, Y.-T., Chen, T.-Y., Hwu, Y. & Margaritondo, G. (2011). *J. Phys. D*, **44**, 232001.